

SUPPORTING INFORMATION

Conformational Evolution of Elongated Polymer Solutions Tailors the Polarization of Light-Emission from Organic Nanofibers

Andrea Camposeo^{1‡*}, *Israel Greenfeld*^{2‡*}, *Francesco Tantussi*^{3,4}, *Maria Moffa*¹, *Francesco Fuso*^{3,4},
Maria Allegrini^{3,4}, *Eyal Zussman*², *Dario Pisignano*^{1,5,*}

¹National Nanotechnology Laboratory of Istituto Nanoscienze-CNR, via Arnesano, I-73100 Lecce (Italy)

²Department of Mechanical Engineering, Technion – Israel Institute of Technology, Haifa 32000, Israel

³Dipartimento di Fisica “Enrico Fermi” and CNISM, Università di Pisa, Largo Bruno Pontecorvo 3, I-56127 Pisa (Italy)

⁴Istituto Nazionale di Ottica INO-CNR, Sezione di Pisa, I-56127 Pisa (Italy)

⁵Dipartimento di Matematica e Fisica “Ennio De Giorgi”, Università del Salento, via Arnesano I-73100 Lecce, (Italy)

*Corresponding Authors: E-mail: andrea.camposeo@nano.cnr.it, green_is@netvision.net.il,
dario.pisignano@unisalento.it

‡These authors contributed equally

1. Theoretical modelling rational

The distinctive photophysical properties of conjugated polymers are strongly affected by the structural conformation of the polymer solid matrix,^{S1-S5} more specifically by the ordering and orientation of chain sections, typically with a conjugation length of ~10-15 monomers in MEH-PPV.^{S1,S6} Individual conjugated polymer chains in a dilute solution can assume various conformations, and hence different optical properties, depending on solvent quality and bonding defects. Theoretically, when defects are not present, the chain is semi-flexible and takes the form of a toroid or rod. However, chemical defects introduced by polymer synthesis and reactivity substitute conjugated links by tetrahedral links along the chain backbone, creating defect coil or cylindrical shapes as a result of the increased flexibility. The defects concentration is in the order of 2.6% to 10% of monomers.^{S1,S2,S5} Generally, in good solvents conjugated chains are swollen and polymer-solvent interactions are dominant, whereas in poor solvents polymer-polymer intrachain and interchain interactions are stronger, favoring aggregation and π - π stacking, respectively.^{S2-S4}

The processing of thin conjugated polymer films from dilute solutions by spin coating, dip coating and casting has a relatively low impact on chain conformations in view of the weak dynamics. Such conformations, extensively investigated both theoretically and experimentally,^{S1-S5} are partly retained after solvent evaporation due to memory effect^{S4} but are still close to the chain equilibrium state. By contrast, electrospinning of semidilute solutions of conjugated polymers is characterized by strong stretching generated by the high electrostatic field, resulting in extended chain conformations and longer conjugation lengths, evidenced by red-shifted optical absorption of fibers and smaller phase separation length scale.^{S7} It is therefore a specific aim of the present study to provide a modeling approach for the conformational evolution of the conjugated polymer chains during electrospinning, including its dependence on solution properties and jet dynamics. It is further intended to describe the impact of the modeled conformation on the solid nanofiber microstructure and photophysical properties in light of MEH-PPV optical observations.

The model is generalized by tuning the degree of chain flexibility with the segmental aspect ratio parameter, and therefore applies to a wide range of linear flexible polymers, including to conjugated polymers with different levels of defects concentration, as well as to fully flexible polymers which are a particular case of the model.

2. Chain conformation in solution

Considering a polymer chain having N rigid segments, each of length $b = nd$ (n spherical beads of diameter d). In a semi-dilute solution, a chain section (subchain) within a correlation volume is essentially unperturbed by other chains, and therefore its end-to-end distance for good solvent can be expressed by Flory's radius:

$$\xi \approx b \left(\frac{v}{b^3} \right)^{2\nu-1} N_s^\nu. \quad (\text{S1})$$

where v is the excluded volume and ν is Flory's exponent. Remembering that a correlation volume encloses a single subchain and that correlation volumes are space filling, the polymer volume fraction in the solution is:

$$\phi \approx \frac{N_s n d^3}{(2\xi/\sqrt{6})^3} = \left(\frac{3}{2}\right)^{3/2} N_s n^{-2} \left(\frac{b}{\xi}\right)^3. \quad (\text{S2})$$

The correlation length is obtained by substituting N_s from Equation (S2) into Equation (S1):

$$\xi \approx b \left(\frac{b^3}{v} \right)^{(2\nu-1)/(3\nu-1)} \left(n^2 \phi \right)^{-\nu/(3\nu-1)}, \quad (\text{S3})$$

with a pre-factor of order unity, $\left(\frac{3}{2}\right)^{3\nu/(6\nu-2)}$. This relation can be obtained also by de Gennes scaling approach. The corresponding number of segments is:

$$N_s \approx \left(\frac{b^3}{v} \right)^{3(2\nu-1)/(3\nu-1)} (n^2\phi)^{-1/(3\nu-1)}. \quad (\text{S4})$$

with a pre-factor of order unity, $(\frac{3}{2})^{3/(6\nu-2)}$. The excluded volume of a non-spherical segment can be expressed by $v \approx b^2d(1-2\chi)$, where χ is Flory's interaction parameter, and therefore:

$$\frac{b^3}{v} \approx \frac{b^3}{b^2d(1-2\chi)} \approx \frac{n}{(1-2\chi)}. \quad (\text{S5})$$

The final expression for the number of segments for good solvent is:

$$N_s \approx \left(\frac{3}{2} \right)^{3/(6\nu-2)} \left(\frac{n}{1-2\chi} \right)^{3(2\nu-1)/(3\nu-1)} (n^2\phi)^{-1/(3\nu-1)}, \quad (\text{S6})$$

which reduces to $N_s \approx (\frac{3}{2})^3 (n^2\phi)^{-2}$ segments for an ideal chain ($\nu = 1/2$).

Figure 4a displays the dependence of N_s on $n^2\phi$, for different solvent types. The θ -solvent curve ($\nu = 1/2$, $\chi = 1/2$) marks the crossover between good and poor solvents, for which the subchain is a random walk of segments (ideal chain conformation). In good solvents ($\nu = 3/5$, $\chi < 1/2$), the subchain is swollen (real chain conformation) and therefore the values of N_s and ξ are lower. The corresponding curve starts at point B', and the athermal limit curve ($\chi = 0$) starts at point B. In poor solvents ($\nu = 1/3$, $\chi > 1/2$), the subchain is shrunk and therefore N_s and ξ are higher, up to the non-solvent limit ($\chi = 1$) where subchains are fully collapsed and phase-separated from the solvent. The corresponding curves start at point B' and B, respectively. N_s is smaller at high aspect ratio (low defects concentration) and is proportional to $n^{-(5-6\nu)/(3\nu-1)}$, i.e. n^{-4} for a θ -solvent and $n^{-1.75}$ for good and athermal solvents.

For chain sections where the excluded volume interaction energy is weak, the conformation is dominated by the thermal energy and is therefore diffusive and ideal. The transition from real to

ideal conformation occurs at the length scale of a thermal blob possessing b^6/v^2 segments. Thus, the number of segments in a thermal blob is:

$$N_{sT} \approx \frac{b^6}{v^2} \approx \left[\frac{n}{1-2\chi} \right]^2, \quad (S7)$$

which reduces to $N_{sT} \approx n^2 \approx \phi^{-2/3}$ for athermal solvents ($\chi = 0$). For solvents other than a θ -solvent, point B' in Figure 4a marks the position where the subchain is of the same length scale as the thermal blob. For larger n (smaller N_s), excluded volume interactions are weak and the thermal energy is dominant; the θ -solvent curve applies and subchains have an ideal conformation. For smaller n (larger N_s), excluded volume interactions are dominant outside the thermal blob; the good solvent or poor solvent curves apply and subchains have an intermediate swollen or collapsed conformation, respectively. The minimal thermal blob size is at the athermal limit (point B), where the athermal solvent or non-solvent curves apply and subchains have a fully swollen or collapsed conformation, respectively. Note that point B slides to the right as the volume fraction increases.

Given the molecular weight or the number of beads in the complete chain, N_{beads} , the chain's number of segments is $N = N_{beads}/n$. The average number of entanglements per chain, $N/N_s \sim n^{3(2-3\nu)/(3\nu-1)}$, decreases for smaller n (i.e. higher defects concentration and chain flexibility) and the solution may turn dilute. Thus, stiffer chains can establish a level of entanglement sufficient for electrospinning at lower concentration and molecular weight. For poor solvents, N_s is close to N , not assuring sufficient entanglements for electrospinning.

The model uses the correlation length as representative for the entanglement length, a chain section between two consecutive entanglements along the chain. In a semi-dilute solution, the elastic modulus of the polymer network is proportional to the number density of entanglement strands. In an athermal solvent, an entanglement strand containing N_e segments is related to the correlation length by $N_e \approx N_e(1)N_s$, where $N_e(1)$ is the number of segments in an entanglement

strand in a melt. Although the entanglement strand length is always longer than the correlation length, in conjugated polymers they are of similar length scale because of the high segmental aspect ratio. Using the known expression for the number of chains within the confinement volume of a single strand in a melt, $P_e \approx (b^3 / v_0) \sqrt{N_e(1)}$, where $v_0 \approx d^2 b$ is the segment volume, the number of strands in a conjugated polymer strand in a melt is:

$$N_e(1) \approx \left(\frac{P_e v_0}{b^3} \right)^2 \approx \left(\frac{P_e}{n^2} \right)^2. \quad (\text{S8})$$

Since $P_e \cong 20$ for all flexible polymers regardless of their segmental aspect ratio, $N_e(1) \approx 1$ when $n \geq \sqrt{P_e} \cong 5$, and therefore practically, for typical defects concentration, $N_e \approx N_s$ as used in the modeling.

3. Network stretching during electrospinning

Using Eq. (S6) and the expression for chain extension, $\xi_{II} \approx (v/v_0)\xi_0 = (a_0/a)^2 \xi_0$,^{S8} the jet radius reduction ratio at full stretching is expressed for good solvents by:

$$\begin{aligned} \frac{a_0}{a_s} &\approx \left(\frac{bN_s}{\xi_0} \right)^{1/2} \approx \left(\frac{n}{1-2\chi} \right)^{(1-2\nu)/2} N_s^{(1-\nu)/2} \\ &\approx \left(\frac{n}{1-2\chi} \right)^{(2\nu-1)/(3\nu-1)} (n^2 \phi)^{-(1-\nu)/[2(3\nu-1)]}. \end{aligned} \quad (\text{S9})$$

Thus, a_0/a_s is reduced as the chain is stiffer, by a factor of $n^{-(2-3\nu)/(3\nu-1)}$, i.e. n^{-1} for a θ -solvent (for which $\nu=1/2$) and $n^{-0.25}$ for good and athermal solvents ($\nu=3/5$).

Finally, in order to find the axial position z_s where subchains approach full extension, it is necessary to estimate the dependence of the velocity parameter z_0 in Eq. (S20) on the parameters that determine the jet rheology, predominantly the solution viscosity η . Additional influencing

parameters, such as the electric field and conductivity, flow rate, and needle diameter, are assumed constant in the current analysis. Sufficiently far from the orifice ($z/z_0 \gg 1$), the jet velocity gradient is proportional to z_0^{-2} (using the exponent $\beta=1$ in Eq. S20). Since, for a given tensile stress (e.g. due to electric field), the gradient is approximately proportional to η^{-1} , the velocity parameter scales as $z_0 \sim \eta^{1/2}$. Written in dimensionless parameters, $z_0/a_0 \sim \eta_{sp}^{1/2}$, where $\eta_{sp} \equiv \eta/\eta_s$ is the specific viscosity (η_s is the solvent viscosity, $\ll \eta$). Hence, The dependence of the axial position on the jet radius (see Eq. S20 in the following Sec. 6) can be approximated by:

$$\frac{z}{a_0} \cong \frac{z_0}{a_0} \left(\frac{a}{a_0} \right)^{-1} \sim \eta_{sp}^{1/2} \frac{a_0}{a}, \quad (\text{S10})$$

where the specific viscosity can be obtained from the known expressions for semi-dilute solutions,^{S9} $\eta_{sp} \approx N^3 \phi^{3/(3\nu-1)}$ for an athermal solvent and $\eta_{sp} \approx N^3 \phi^{14/3}$ for a θ -solvent (prefactors are omitted).

Using the radius reduction ratio from Equation (S9) and the viscosity expressions, z_s scales as:

$$\frac{z_s}{a_0} \sim N^{3/2} \begin{cases} \phi^{\frac{\nu+2}{2(3\nu-1)}} & \text{athermal solvent} \\ \phi^{11/6} & \theta \text{ solvent,} \end{cases} \quad (\text{S11})$$

depicted in Figure 6a. The concentration dependence of z_s is $\phi^{1.63}$ for an athermal solvent and $\phi^{1.83}$ for a θ -solvent. Note that this expression is written for fully flexible chains ($n=1$), with the intention to demonstrate the trends of the dependence on the concentration, solvent quality, and molecular weight.

4. Nanofiber optical properties

The absorption spectra are measured by using a UV/visible spectrophotometer (Lambda950, PerkinElmer) and an integrating sphere (Labsphere). PL spectra are acquired by exciting the nanofibers with a diode laser ($\lambda=405$ nm, polarization parallel to the fiber axis) and collecting the emission through a fiber-coupled monochromator (iHR320, JobinYvon) equipped with a charged coupled device (Jobin Yvon). In Figure S1a we compare the absorption spectrum of a mat of MEH-PPV nanofibers with a reference spincoated film. The film displays a maximum absorption at about 510 nm, whereas a peak red shift of about 5 nm is measured for fibers, which indicates a slight increase of the effective conjugation length attributable to a more ordered molecular packing.^{S7} Moreover, the absorption spectrum of the fibers is also broader compared to the film sample. The full width at half maximum (FWHM) of the fiber absorption spectrum is 150 nm, whereas a FWHM of 120 nm is measured for the film. Such broadening has been also observed in other electrospun MEH-PPV nanofibers and attributed to a more inhomogeneous environment.^{S7}

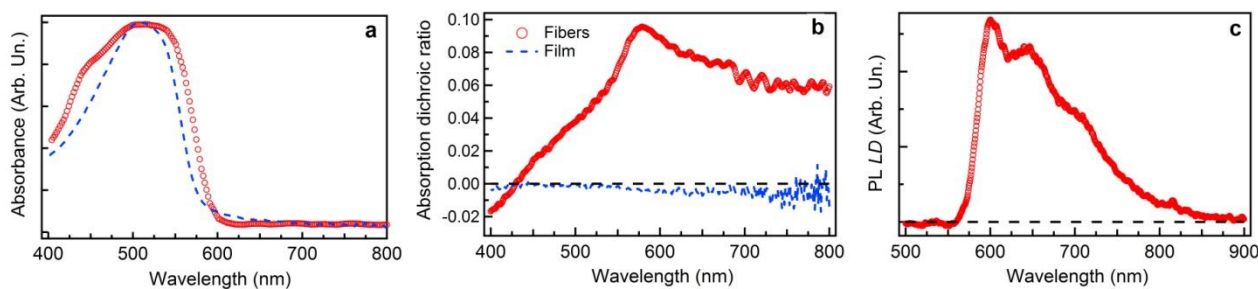


Figure S1. (a) Absorption spectra of a reference MEH-PPV film (dashed line) and of the nanofibers (circles). (b) Dichroic ratio spectra of fibers (empty circles) and reference spincoated films (dotted line). The spectra are obtained by measuring the polarized absorption spectra, with incident light polarization aligned parallel (A_{\parallel}) and perpendicular (A_{\perp}) to the fiber alignment axis, respectively. The dichroic ratio is then calculated by: $\gamma = (A_{\parallel} - A_{\perp}) / (A_{\parallel} + A_{\perp})$. The spectrum of the reference film clearly displays average null values. (c) PL linear dichroism spectrum (LD_{PL}), calculated by PL spectra exciting the fibers with the laser polarized along the fiber axis and collecting the PL through

a polarization filter with axis parallel ($I_{PL//}$) and perpendicular ($I_{PL\perp}$) to the fiber axis, respectively (i.e., $LD_{PL} = I_{PL//} - I_{PL\perp}$). The horizontal black dashed lines mark null values.

The absorption dichroic ratio spectrum is shown in Figure S1b. The plot, obtained from polarized absorption measurements performed on uniaxially aligned MEH-PPV nanofibers, evidences a predominant absorption for light polarized along the fiber longitudinal axis, a fingerprint of a preferential alignment of the polymer backbones along the fiber length. The values are peaked at about 575 nm, corresponding to the (0-0) vibronic replica of the π - π^* electronic transition. Figure S1c displays the photoluminescence (PL) linear dichroism defined as the difference between the intensity of the light emitted by fibers with polarization parallel or perpendicular to the fiber axis ($LD_{PL} = I_{PL//} - I_{PL\perp}$). The measured polarization anisotropy of the emission further supports the anisotropic packing of MEH-PPV molecules in the electrospun fibers.

5. Near-field Optical Microscopy set-up

The analysis of the optical activity at the local scale is performed by using a polarization-modulated scanning near-field optical microscope (SNOM) developed on the basis of a multi-purpose head.^{S10} The instrument operates in the emission-mode: the sample interacts with the near-field produced by a tapered optical fiber probe (50 nm nominal diameter apical aperture). Radiation is collected below the sample by an aspheric lens and directed onto a miniaturized photomultiplier. The configuration is hence similar to that of conventional optical transmission measurements, but for the use of the near-field, the key component enabling spatial resolution below the diffraction limit.

Producing maps of the linear dichroism requires the ability to measure the response of the sample upon excitation with controlled polarization states. To this aim, polarization modulation (PM) methods are typically employed.^{S11} The main motivation is the long duration of SNOM scans,

that makes mechanical drifts likely to occur. As a consequence, subsequent scans of the same region recorded with rotated polarizations can be hardly carried out. PM circumvents the problem by continuously manipulating the polarization state at every point of a single scan. In addition, signal-to-noise ratio is improved thanks to demodulation through lock-in amplifiers, that makes the measurement of small dichroism variations feasible.^{S12}

Core of the polarization modulation system is a photoelastic modulator (PEM, Hinds Instruments PEM-100) which acts as a waveplate whose retardation is periodically modulated at $f = 50$ kHz.^{S13} As shown in Fig. S2, the modulator is followed by a $\lambda/4$ waveplate. Being the linear polarization of the excitation laser directed at 45° with respect to the PEM optical axes, the polarization entering the $\lambda/4$ waveplate is periodically modified through linear to elliptical and circular states. After passage through the waveplate, oriented at -45° with respect to the PEM axes, the polarization is converted back to linear, but its in-plane direction gets now periodically modulated. In typical operating conditions, the freely adjustable, maximum retardation produced by the PEM is set to $A = \pi$. Consequently, the whole range of directions (0 - 360°) is spanned two times in a single modulation period $T = 1/f$. Lock-in demodulation at twice the frequency f brings information (hereafter called AC signal) on the response of the sample to polarized radiation. Since the intensity of the signal collected by the photodetector can be affected by a number of effects, including instrumental drifts, variations in the coupling efficiency with the near-field, as well as polarization-independent absorption, the AC signal must be normalized. A reference can be easily obtained by averaging the photodetector output over all polarization states. In our setup this is achieved by using an independent lock-in amplifier connected at the photo-detector output and referenced to a slow ($f' < f/10$) amplitude modulation of the excitation laser, that produces a signal (hereafter called DC) time-averaged over all polarization states. The normalized AC/DC signal contains information on the linear dichroism of the sample.

Measurements at the local scale involve the use of near-field radiation. Different previous reports have demonstrated the ability of polarization modulated SNOM in achieving a polarization-

related contrast mechanism and in determining the optical activity of a variety of samples.^{S14-S21}

However, especially when near-field probes based on tapered optical fibers are used, as in our case, special care must be devoted to account for the residual optical activity. In fact, birefringence of the fiber, as well as any other spurious effect stemming from the optical bench components (mirrors, beam splitters), can heavily affect the results, in particular their quantitative evaluation. In order to remove those unwanted contributions, prior to the measurements we analyze bare substrates, expected to show negligible optical activity. Both demodulated signals (lock-in outputs) and time-resolved data are compared to results obtained through calculations aimed at simulating the polarization-dependent behavior of the optical components in the experimental chain. Such calculations have been based on the Jones matrix formalism (more complicated methods, such as those based on the Mueller formalism, did not lead to significant advantages).

Within this frame, the time-dependent polarization of the light at the PEM output can be represented by the following vector, whose components are the electric field amplitude along two mutually orthogonal in-plane directions (x and y) in the reference frame of the optical bench:

$$V = \frac{1}{\sqrt{2}} \begin{pmatrix} e^{i\Delta(t)} \\ 1 \end{pmatrix}, \quad (\text{S12})$$

with $\Delta(t) = A\sin(2\pi ft + \delta)$, where δ represents a constant phase factor accounting for instrumental delays. The modifications to the polarization produced by each component are described by 2×2 matrices. The whole system behavior is then given by the product of all considered matrices.

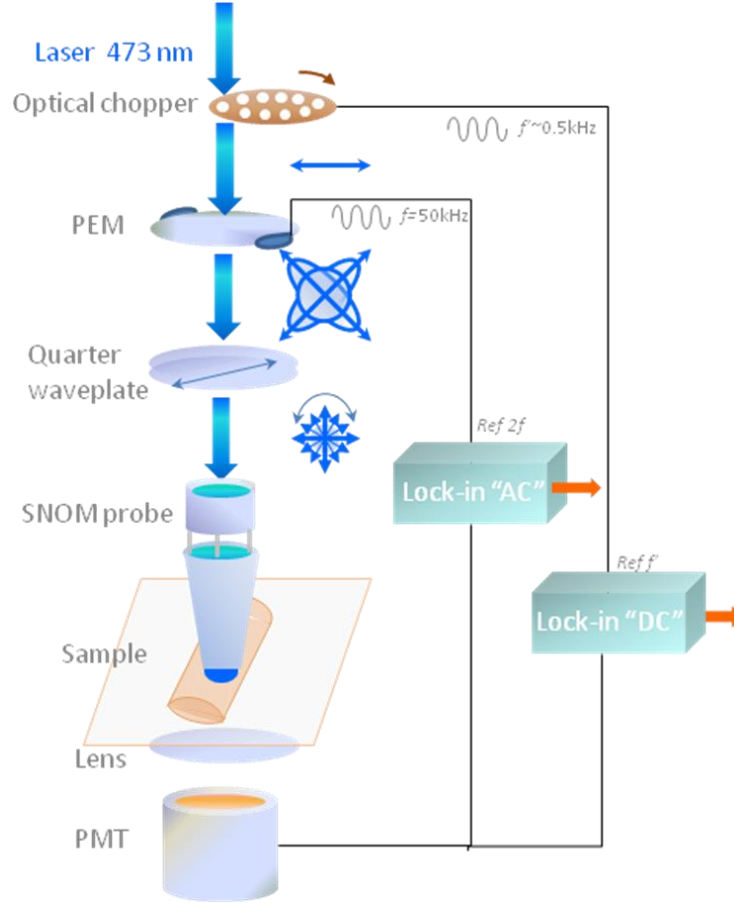


Figure S2. Representation of polarization modulated SNOM. Close to some of the optical components, the polarization of the excitation radiation is schematically shown. Note that, in the actual setup the optical chopper, depicted as a rotary wheel, is replaced by an acousto-optic shutter in order to prevent mechanical noise on the microscope table.

For instance, the $\lambda/4$ waveplate, aligned as in our setup, can be described by the following matrix:

$$W = \frac{1}{\sqrt{2}} \begin{pmatrix} \cos \theta & -\sin \theta \\ \sin \theta & \cos \theta \end{pmatrix} \begin{pmatrix} 1 & 0 \\ 0 & i \end{pmatrix} \begin{pmatrix} \cos \theta & \sin \theta \\ -\sin \theta & \cos \theta \end{pmatrix}, \quad (\text{S13})$$

with $\theta = -\pi/4$. A generic birefringent component, with its optical axes rotated by a generic angle β with respect to the reference system, can be represented by the matrix M :

$$M = \frac{1}{\sqrt{2}} \begin{pmatrix} \cos \beta & -\sin \beta \\ \sin \beta & \cos \beta \end{pmatrix} \begin{pmatrix} e^{-i\Delta\phi} & 0 \\ 0 & 1 \end{pmatrix} \begin{pmatrix} \cos \beta & \sin \beta \\ -\sin \beta & \cos \beta \end{pmatrix}, \quad (\text{S14})$$

where $\Delta\phi$ is the optical retardation produced by the birefringent component. The matrix M can conveniently describe the spurious birefringence induced by the probe.

The components of the electric field, D , collected by the photodetector (in the absence of any optically active sample) are given by the product:

$$D = MWV, \tag{S15}$$

which is time-dependent due to the explicit dependence of V on t . Assuming photodetector response independent of polarization, as confirmed by specific calibration measurements showing negligible variations of the output signal for radiation polarized along two mutually orthogonal directions, the intensity $I(t) = |D(t)|^2$ can then be simulated and compared to the signal measured by the photodetector in the experiment, duly amplified and acquired by a fast digital oscilloscope averaging over many modulation cycles in order to enhance the signal-to-noise ratio. By adjusting the calculation parameters to achieve the best agreement between the simulated and the observed temporal shape of the signal, the retardation $\Delta\phi$ can be estimated.

In our experiments we select probes showing a residual birefringence, $\Delta\phi < 0.1$ rad. Moreover, since the birefringence can be altered by naturally occurring mechanical stresses of the fiber, particular care is taken to keep stable the eventual mechanical stress and to minimize long term drifts, as experimentally confirmed by measuring the AC signal fluctuations in scans of bare substrates (measured well below 10% on the duration of a whole scan, typically lasting for several tens of minutes).

In order to have an additional confirmation of the suitability of the selected probes, further tests are carried out in which a linear polarizer is used as SNOM sample. Then, we replace the PEM and $\lambda/4$ assembly with a $\lambda/2$ waveplate. Rotating such waveplate, we can obtain a linear polarization aligned along a variable direction at the entrance of the probe, and use the photodetector output to carry out an analysis mimicking the crossed-polarizer configuration. The probes used in our experiments feature extinction ratios of the order of 10^1 - 10^2 , ruling out possible polarization scrambling effects.

Once the spurious birefringence has been characterized, the dichroism of the sample can be determined by using a matrix S describing a generic linearly dichroic material with its axes rotated at a generic angle α :

$$S = \begin{pmatrix} \cos \alpha & -\sin \alpha \\ \sin \alpha & \cos \alpha \end{pmatrix} \begin{pmatrix} e^{-k_1 z} & 0 \\ 0 & e^{-k_2 z} \end{pmatrix} \begin{pmatrix} \cos \alpha & \sin \alpha \\ -\sin \alpha & \cos \alpha \end{pmatrix}, \quad (\text{S16})$$

where k_1 and k_2 are the absorption coefficients for radiation polarized along two mutually orthogonal directions representing the optical axes of the sample, and z is the thickness of the absorbing material, that can be experimentally inferred by the topography maps. The response of the whole system produces the time-dependent electromagnetic field D_S :

$$D_S = SMWV. \quad (\text{S17})$$

In order to compare with experimental data (at a fixed point of the scan, to remove the dependence on z), lock-in demodulation at frequency $2f$ (or f) of the intensity $I_S(t) = |D_S(t)|^2$ measured by photodetector can be easily simulated, corresponding in practice to the measured AC/DC ratio. Thanks to the use in the experiment of dual lock-in amplifiers, any possible dephasing between the reference and the signal modulation, for instance caused by the parameter δ (see Eq. S12), can be neglected.

The absorption coefficients can in turn be linked to the dichroic ratio of the material:

$$\gamma = \frac{I_{\parallel} - I_{\perp}}{I_{\parallel} + I_{\perp}} \quad (\text{S18})$$

where

$$I_{\parallel} = I_0 e^{-k_1 z} \quad \text{and} \quad I_{\perp} = I_0 e^{-k_2 z} \quad (\text{S19})$$

We note that the above defined dichroic ratio can get either positive or negative values, depending on whether $k_1 < k_2$, or vice versa. The ability to retrieve the sign of γ is indeed very useful when the spatial distribution of the dichroic behavior in isolated systems has to be investigated, as in our case. In fact, this allows to identify regions with radically different polarization-dependent absorption, as due, for instance, to peculiar alignment of molecules.

The procedure leads to a calibration curve where the simulated AC/DC ratio is plotted as a function of γ that can be used to put a scale bar into the experimentally produced maps. Figure S3 shows an example of the resulting curve. We estimate the uncertainty of our procedure, accounting for all the error sources in our simple calculation model, of the order of $\pm 10\%$.

As shown in Fig. S3, non-zero AC/DC is expected at $\gamma = 0$. The occurrence of such a background pedestal, which is an obvious consequence of the spurious optical activity of the optical bench, is well confirmed in the experimental maps, where the bare substrate actually displays non-zero AC/DC. Thanks to the calibration curve, the effect disappears in the maps calibrated in units of γ , as shown in Fig. 3b.

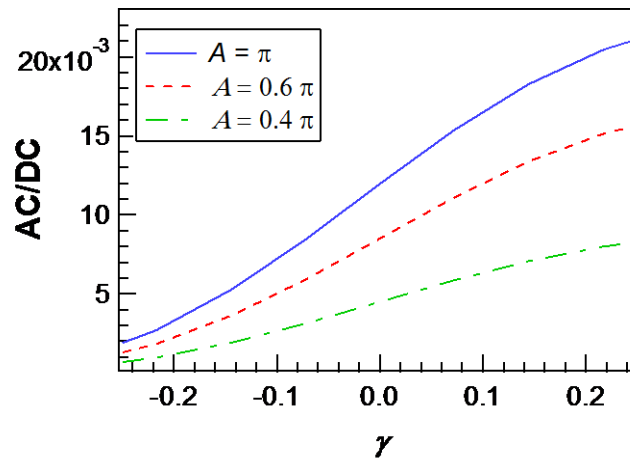


Figure S3. Example of a calibration curve, as defined in the text, relating the simulated AC/DC ratio with the dichroic ratio of the material. In this example, which fits experimental data, the residual birefringence of the probe is computed as $\Delta\phi = 0.06$ rad and the angle α appearing in Eq. S16 is $\alpha \sim \pi/2$. Different curves are calculated assuming different values of the maximum PEM retardation A , as specified in the legend.

We note also that the angle α entering Eq. S16 is measured in the in-plane directions (x', y') of the sample reference frame, different from the reference frame (x, y) used to determine all the other angular quantities appearing in Eqs. S13, S14. The rotation of the reference axes can be

experimentally estimated by selecting a constant linear polarization at the entrance of the fiber probe with a known direction, by placing a rotatable linear polarizer in front of the photodetector and by looking at the maximum (or minimum) signal. Being the photodetector mounted in the SNOM microscope, the direction of the reference axes in the SNOM frame can be deduced. However, such a technique can be rather cumbersome from the experimental point of view, in particular because it requires removal and replacement of the sample. An *in-situ* procedure can be carried out instead, based on the circumstance that the calibration curves depend on the maximum retardation A set for the PEM. This is shown, for instance, in Figure S3, where calibration curves for three different choices of A are plotted. Hence, by repeating the same SNOM scan with different A -values and comparing the so-obtained AC/DC maps, it is possible to infer on the value of α entering Eq. S16. For the measurements shown in the paper, α is slightly larger than $\pi/2$. Being the nanofiber axis roughly aligned along the vertical direction of the scan, measurements are referenced to polarization directions aligned roughly along and across the nanofiber, that is, k_1 and k_2 roughly corresponds to absorption along the longitudinal and radial directions of the fiber, respectively. As a consequence, negative and positive dichroic ratios correspond to prevalent absorption of radiation polarized along or across the fiber, respectively.

6. Imaging of the electrospinning jet profile

For imaging the polymer jet profile a high speed camera (Photron, FASTCAM APX RS, 1024 pixel \times 1024 pixel, 10000 frame s^{-1}) coupled to a stereomicroscope (Leica MZ 12.5) is used. A typical image of the measured jet shape is shown in Figure S4. The dependence of the jet radius, a , on the axial coordinate, z , is modelled by the following relation:^{S8,S22}

$$\left(\frac{a_0}{a}\right) \cong \left(1 + \frac{z}{z_0}\right)^\beta, \quad (\text{S20})$$

Fitting the jet profile to Equation (S20) provides values of $z_0 = 22 \mu\text{m}$, and $\beta = 0.94$, using the initial radius $a_0 = 96 \mu\text{m}$.

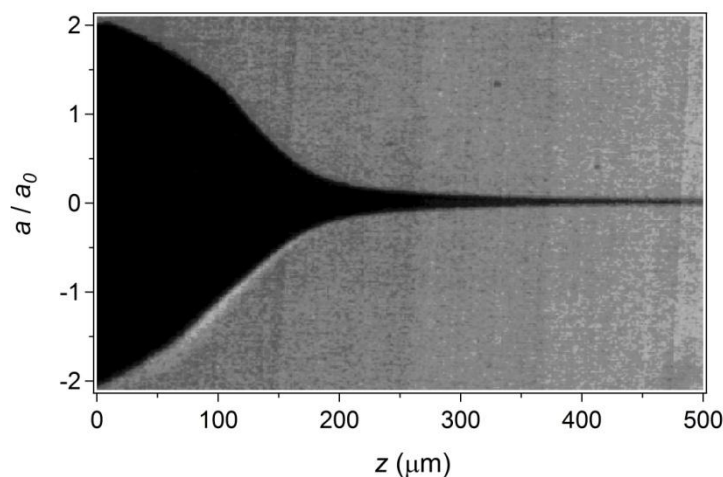


Figure S4. Typical image of a jet profile used to calculate the radius dependence on the axial coordinate, z (Eq. S20). $a_0 = 96 \mu\text{m}$.

References

- S1. D. H. Hu, et al. *Nature*, **2000**, *405*, 1030-1033.
- S2. Y. Ebihara, and M. Vacha, *J. Phys. Chem. B*, **2008**, *112*, 12575-12578.
- S3. T. Q. Nguyen, V. Doan, and B. J. Schwartz, *J. Chem. Phys.*, **1999**, *110*, 4068-4078.
- S4. R. F. Cossiello, M. D. Susman, P. F. Aramendia, and T. D. Z. Atvars, *J. Lumin.*, **2010**, *130*, 415-423.
- S5. S. C. Shie, C. K. Lee, C. C. Hua, and S. A. Chen, *Macromolecular Theory and Simulations*, **2010**, *19*, 179-189.
- S6. D. H. Hu, J. Yu, and P. F. Barbara, *J. Am. Chem. Soc.*, **1999**, *121*, 6936-6937.

- S7. D. Li, A. Babel, S. A. Jenekhe, and Y. Xia, *Adv. Mater.*, **2004**, *16*, 2062-2066.
- S8. I. Greenfeld, A. Arinstein, K. Fezzaa, M. H. Rafailovich, and E. Zussman, *Phys. Rev. E*, **2011**, *84*, 041806.
- S9. M. Rubinstein and R. H. Colby, *Polymer physics*. Oxford University Press: Oxford; New York, 2003; p. xi, p. 440.
- S10. P. Gucciardi, M. Labardi, S. Gennai, F. Lazzeri, and M. Allegrini, *Rev. Sci. Instrum.*, **1997**, *68*, 3088.
- S11. P. Gucciardi, R. Micheletto, Y. K. Kawakami, and M. Allegrini, in “Near-field optical microscopy for imaging of polarization anisotropy in photonic nanostructures”, edited by B. Bhushan and H. Fuchs (Springer, Berlin Heidelberg New York, 2006) Chap. 10, pp. 321–360.
- S12. A. F. Drake, *J. Phys. E: Sci. Instrum.*, **1986**, *19*, 170.
- S13. B. Wang, *SPIE Proceedings*, **1998**, *3424*, 120.
- S14. M. Vaez-iravani, and R. Toledo Crow, *Appl. Phys. Lett.*, **1993**, *63*, 138.
- S15. T. Lacoste, T. Huser, R. Prioli, and H. Heinzelmann, *Ultramicroscopy*, **1998**, *71*, 333.
- S16. L. Ramoino, L. et al., *Rev. Sci. Instrum.*, **2002**, *73*, 2051.
- S17. Ambrosio, A. et al., *Nanotechnology*, **2004**, *15*, 5270.
- S18. R. Micheletto, Y. Kawakami, C. Manfredotti, Y. Garino, and M. Allegrini, *Appl. Phys. Lett.*, **2006**, *89*, 121125.
- S19. R. Micheletto, M. Allegrini, and Y. Kawakami, *J. Opt. A: Pure Appl. Opt.*, **2007**, *9*, 431.
- S20. M. Savoini, P. Biagioni, L. Duò, M. Finazzi, *Opt. Lett.*, **2009**, *34*, 761.
- S21. F. Tantussi, et al. *Appl. Phys. Lett.*, **2012**, *100*, 08313.
- S22. I. Greenfeld, K. Fezzaa, M. H. Rafailovich, and E. Zussman, *Macromolecules*, **2012**, *45*, 3616-3626.